Journal of Solid State Chemistry **157,** 123–133 (2001)
doi:10.1006/jssc.2000.9051, available online at http://www.idealibrary.com on IDEAL®

$BiMn_6PO_{12}$, A New Bismuth Manganese II/III Oxyphosphate with an Original Manganese–Oxygen Cubic Network

O. Cousin, O. Mentré, M. Huvé, and F. Abraham[1]

Laboratoire de Cristallochimie et Physicochimie du Solide, UPRESA CNRS 8012, ENSCL, Université des Sciences et Technologies de Lille, B. P. 108, 59652 Villeneuve d'Ascq Cedex, France

Received July 27, 2000; in revised form November 7, 2000; accepted December 8, 2000

A new bismuth manganese oxyphosphate, $BiMn_6PO_{12}$, with an original cubic structure has been synthesized by solid state reaction from Bi_2O_3, MnO_2, and $(NH_4)_2HPO_4$ or $BiPO_4$ and Mn_3O_4 mixtures. Its crystal structure has been determined from single-crystal X-ray diffraction data. It crystallizes in the cubic system with space group $Fm\bar{3}m$ and unit cell parameter $a = 9.626(1)$ Å, $Z = 4$. A full-matrix least-squares refinement yielded $R = 0.044$ and $R_w = 0.045$ for 131 independent reflections with $I > 2\sigma(I)$ collected on a Philips PW100 diffractometer (Mo$K\alpha$ radiation). The structure of $BiMn_6PO_{12}$ is characterized by a three-dimensional network of manganese–oxygen bonds. The oxygen atoms form a rhombicuboctahedron. The manganese atoms occupy two-thirds of the square faces of this polyhedron and are at the vertices of cuboctahedra. Manganese and oxygen atoms form a $Mn_{12}O_{24}$ cage, which constitute the strong basic element of the global building. The PO_4 tetrahedron is located within this cage and can be moved between two equivalent orientations. The connection between $Mn_{12}O_{24}$ entities created little cubic holes occupied by bismuth atoms. In this compound all the manganese atoms are crystallographically equivalent and the mean oxidation state of manganese is +2.67. A superstructure, which could be due to PO_4 orientations ordering, was evidenced by an electronic diffraction study. $BiMn_6PO_{12}$ exhibits complicated magnetic behavior with several magnetic transitions both in the paramagnetic state and in the low-temperature ordered state. © 2001 Academic Press

INTRODUCTION

Synthesis and characterization of new bismuth-based compounds exhibiting various interesting properties is one of the major objectives of our laboratory. We have already succeeded in the preparation of several intensively studied bismuth–3*d* transition metal oxides such as Bi_2CuO_4 (1), a three-dimensional antiferromagnetic material that attracts special attention in fundamental physics, and $Bi_4V_2O_{11}$ (2), the parent of the oxygen ion superconductors family, BIMEVOX (3). The investigation of Bi_2O_3–MO–P_2O_5, M = Cu, Ni, ternary systems (4, 5) allowed us to prepare new interesting bismuth–3*d* metal oxyphosphates. For M = Cu, $BiCu_2PO_6$ was first isolated (6), belonging to the large series of compounds with formula BiM_2XO_6 (M = Mg, Cu, Zn, Cd, Ca, Pb; X = P, V, As) (7–14) and $Bi_4Cu_3P_2O_{14}$ (15), isotypic with $Bi_4Cu_3V_2O_{14}$ (4, 16). For M = Ni, the oxyphosphate $BiNiPO_5$ has been structurally characterized (17), and the isotypic cobalt compound $BiCoPO_5$ was obtained (18, 19). We have recently undertaken the investigation of the Bi–Mn–P–O system, which proved to be very complicated due to the various oxidation states possible for manganese but of great interest owing to the attractive properties of mixed valence manganese oxides such as the colossal magnetoresistance (20). This paper describes the preparation and the structural approach of a new bismuth manganese oxyphosphate, $BiMn_6PO_{12}$, that contains mixed-valence manganese and exhibits a very original structure. The magnetic behavior of this compound is also reported.

EXPERIMENTAL

Syntheses

The oxides Bi_2O_3 (Riedel), MnO_2 (Aldrich), Mn_3O_4 (Johnson Matthey), and PbO (Prolabo), and the phosphate $(NH_4)_2HPO_4$ (Fluka) were used as starting materials.

For single-crystal preparation a mixture of Bi_2O_3, PbO, MnO_2, and $(NH_4)_2HPO_4$ was progressively heated to 875°C in a gold crucible with intermediate grindings; after a 2-h stage at this temperature, the batch was cooled to room temperature at 1.5°C/h. The product contained two components present as single crystals of quality suitable for diffraction study: brown needle-like crystals (tetragonal, $a = 13.364(2)$ $c = 5.491(2)$ Å), which are under investigation, and black broken cubes of the title compound. The former phase was the major component in the product as confirmed by the powder X-ray diffraction pattern of the

[1] To whom correspondence should be addressed. E-mail: abraham@ensc-lille.fr.

0022-4596/01 $35.00

crushed bulk sample. Cubic crystals contained Bi, Mn, and P in an atomic ratio 1:6:1 and no lead was revealed from an energy-dispersive spectroscopic analysis using a JEOL JSM-5300 scanning microscope equipped with a PGT digital spectrometer.

For the preparation of polycrystalline powder two methods were used. In the first one, stoichiometric amounts of Bi_2O_3, MnO_2, and $(NH_4)_2HPO_4$ were first heated to 300°C at a rate of 30°C/h, maintained 10 h at 300°C, then heated to 500°C, kept at this temperature for 10 h, and heated to a final temperature ranging from 850 to 910°C. At each stage, the mixture was reground. Whatever the final firing temperature, the product was a mixture of $BiMn_6PO_{12}$ and a badly crystallized unidentified phase. Starting from MnO_2, the reduction of Mn^{4+} to Mn^{3+} and Mn^{2+} is spontaneous at the synthesis temperature. The spontaneous reduction of manganese to a Mn^{2+}/Mn^{3+} mixture is known, for example, for any simple manganese oxide which leads to Mn_3O_4 when it is heated to about 1000°C in air. The studied compound can be appropriately formulated $BiPO_4$–$2Mn_3O_4$; thus, in the second preparation, $BiPO_4$, synthesized from Bi_2O_3 and $(NH_4)_2HPO_4$ at 850°C, and Mn_3O_4 were used as starting materials. Stoichiometric amounts of the raw materials were heated either in an ambient atmosphere in a gold boat or under vacuum in a silica tube for 48 h at 900°C. Unfortunately, the product was also a mixture of $BiMn_6PO_{12}$ and of the unidentified phase. Pure $BiMn_6PO_{12}$ was obtained by washing the product with 65% nitric acid to dissolve the second phase. Purity was checked by density measurements performed using an automated Micrometrics Accupyc 1330 helium pycnometer in a 1-cm^3 cell and X-ray controlled as follows.

Structure Determination

The X-ray powder pattern of the washed sample obtained with a Siemens D 5000 diffractometer (Cu$K\alpha$ radiation) equipped with a monochromator was easily indexed with a F-cubic lattice. The unit cell parameter was refined to the value 9.626(1) Å. The figure of merit as defined by Smith and Snyder (21) was $F_{17} = 113$ (0.0088, 17). The powder X-ray diffraction pattern is shown in Fig. 1, corresponding to the data reported in Table 1. A black, nearly spherical single crystal was selected for the structure determination. The intensity data were collected on a Philips PW1100 automated diffractometer. Conditions for data collection are given in Table 2. The intensity of each reflection was corrected for background and for Lorentz and polarization effects. Absorption corrections were performed assuming a perfect spherical geometry for the crystal and an average radius of 60 μm.

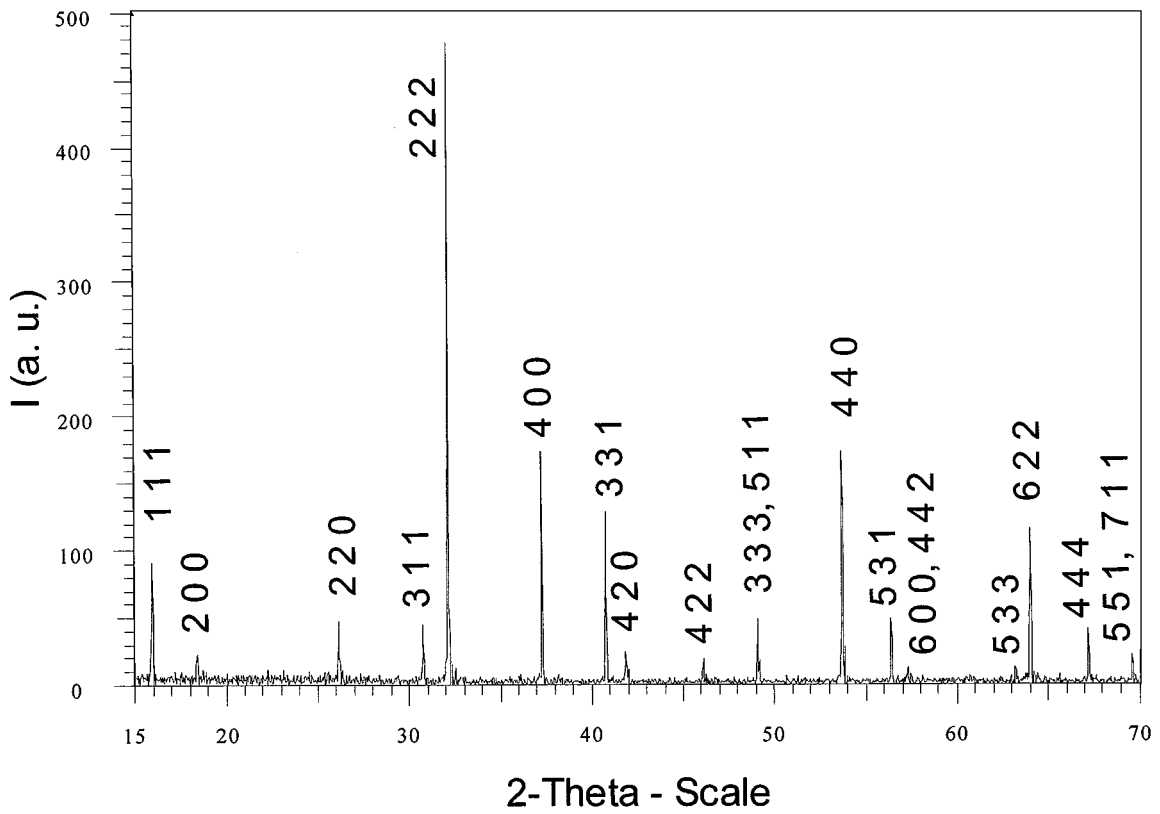

FIG. 1. The $BiMn_6PO_{12}$ X-ray powder pattern of acid-washed $BiMn_6PO_{12}$ collected using a Cu$K\alpha$ radiation.

TABLE 1
Observed and Calculated X-Ray Powder Diffraction Pattern for $BiMn_6PO_{12}$

hkl	2θ obs.	2θ calc.	Int.
111	15.919	15.917	19
200	18.414	18.402	5
220	26.137	26.146	10
311	30.761	30.764	9
222	32.159	32.169	100
400	37.320	37.318	36
331	40.800	40.810	27
420	41.920	41.921	5
422	46.161	46.142	4
333, 511	49.122	49.121	10
440	53.816	53.811	36
531	56.480	56.493	10
600, 442	53.842	53.831	1
533	63.311	63.307	1
622	64.104	64.056	23
444	67.321	67.315	8
551, 711	69.682	69.685	4

Note. $\lambda = 1.54056$ Å, refined zero-point correction 0.0078(2) for θ; $a = 9.626(1)$ Å, $F_{17} = 113$ (0.0088, 17).

The structure was solved in the centrosymmetric $Fm\bar{3}m$ space group by direct methods using the SHELXS program (22), which localizes bismuth atoms in a 4*a* site (0, 0, 0), manganese atoms in a 24*d* position $(0, \frac{1}{4}, \frac{1}{4})$ and other atoms in a 32*f* site (0.14, 0.14, 0.14). Owing to the distances, this site was occupied by oxygen atoms. The positions of P and remaining oxygen atoms were deduced from subsequent refinements and Fourier syntheses. The P atoms occupy a 4*b* site $(\frac{1}{2}, \frac{1}{2}, \frac{1}{2})$ and the remaining oxygen atoms are randomly distributed on a half-occupied 32*f* site. Refinement in the non-centrosymmetric $F\bar{4}3m$ space group did not improve the results; in fact, two independent oxygens must be introduced in two half-filled 16*e* positions related by an inversion center to achieve an acceptable convergence. The full-matrix least-squares refinement was performed with a local modification of the SFLS-5 program (23). The atomic scattering factors for neutral atoms were taken from the "International Tables for X-ray Crystallography" (24) and the values for the anomalous dispersion corrections from Cromer and Liberman (25). Refinement of atomic positional parameters and anisotropic displacements yielded to final $R = 0.044$ and $R_w = 0.045$ for 131 independent reflections. The atomic positions and equivalent isotropic displacement factors are reported in Table 3. Anisotropic displacement parameters are given in Table 4.

Electronic Diffraction

Electron diffraction patterns were obtained with a Jeol 200CX microscope. The materials were crushed and dispersed on a holey carbon film deposited on a copper grid.

Magnetic Measurements

The magnetic properties were measured using a superconducting quantum interference device (SQUID) magnetometer (Quantum Design, MPMS). The magnetic susceptibility was measured from 300 to 2 K using pure nitric acid washed $BiMn_6PO_{12}$ powder (18 mg) with an external field of 100 Oe. The magnetization was studied on the same sample with an external field of -5.5×10^4 to 5.5×10^4 Oe.

RESULTS AND DISCUSSION

Description and Discussion of the Crystal Structure

Selected bond lengths and bond angles are listed in Table 5.

The oxygen atoms O(1) constitute a $O(1)_{24}$ rhombicuboctahedron formed from 18 square planes and 8 equilateral triangles with an O(1)–O(1) distance of 2.78 Å linked by edge sharing (Fig. 2a). Each entity is connected by two-thirds of the $O(1)_4$ squares (those that share an edge with

TABLE 2
Crystal Data, Intensity Collection, and Structure Refinement Parameters for $BiMn_6PO_{12}$

Crystal data	
Crystal symmetry	Cubic
Space group	$Fm\bar{3}m$
Unit cell refined on powder	$a = 9.626(1)$ Å
Volume	891.9 Å^3
Z	4
Calculated density	$\rho = 5.67$ g cm^{-3}
Measured density	$\rho = 5.62(2)$ g cm^{-3}
Data collection	
Equipment	Philips PW 1100
Radiation Mo$K\alpha$	0.7107
Scan mode	ω–2θ
Scan width/degrees	0.9
Recording angular range (°)	2–35
Standard reflections	$\bar{3}\bar{1}3$, $\bar{2}\bar{2}2$, 133
Recording reciprocal space	$-15 \le h \le 15$, $-15 \le k \le 15$, $0 \le l \le 15$
Number of measured reflections	2011
Number of reflections with $I > 2\sigma(I)$	2009
Number of independent reflections	131
μ (cm^{-1}) (for $\lambda_{K\alpha} = 0.7107$ Å)	282.4
Transmission factor range	0.019–0.033
R merging factor	0.103
Refinement parameters	
Number of refined parameters	12
Goof = S(goodness of fit)	4.3
$R = \sum[\lvert F_o\rvert - \lvert F_c\rvert]/\sum\lvert F_o\rvert$	0.044
$R_w = [\sum w(\lvert F_o\rvert - \lvert F_c\rvert)^2/\Sigma F_o^2]^{1/2}$ with $w = 1/\sigma(F_o)$	0.045
Max., min, $\Delta\rho$ e Å^{-3}	2.32, -2.79

TABLE 3
Atomic Positions and Equivalent Isotropic Displacement Parameters for $BiMn_6PO_{12}$

Atom	Site	Occupancy	x	y	z	B_{eq} (Å^2)
Bi	4*a*	1	0	0	0	0.96(2)
Mn	24*d*	1	0	$\frac{1}{4}$	$\frac{1}{4}$	0.71(3)
P	4*b*	1	$\frac{1}{2}$	$\frac{1}{2}$	$\frac{1}{2}$	0.29(4)
O(1)	32*f*	1	0.1445(6)	0.1445(6)	0.1445(6)	1.81(8)
O(2)	32*f*	0.5	0.4086(7)	0.4086(7)	0.4086(7)	0.49(9)

Note. Equivalent isotropic temperature factors are computed according to the relation $B_{eq} = 4/3\sum_{ij}\beta_{ij}a_ia_j$.

a triangle) to 12 other entities to form a three-dimensional oxygen network (Fig. 2b). The centers of the shared $O(1)_4$ squares are occupied by manganese atoms forming a perfect cuboctahedron (Fig. 2c); the equilateral triangles are empty. The three-dimensional Mn_6O_8 framework thus formed releases two kinds of cavities.

The large ones at the center of the $Mn_{12}O_{24}$ rhombicuboctahedra are occupied by PO_4 tetrahedra (Fig. 2d). In this mean structure the PO_4 tetrahedra randomly occupy two equivalent positions related by an inversion center. Bi^{3+} ions are located at the center of the little cubic holes resulting from the connection of six $Mn_{12}O_{24}$ rhombicuboctahedra (Fig. 3). Moreover, the examination of thermal factors shows a strong discrepancy between the B_{eq} of oxygen atoms. Astonishingly, the displacement parameter for the O(2) atoms, which are disordered, is lower than the value for the perfectly ordered O(1) atoms, although the cage formed by the 24 O(1) atoms containing the network of Mn atoms constitutes the strong basic element of the global building. To find an explanation for this observation, it is necessary to take care of the situation of Bi atoms, which are probably not strictly on the 4*a* site. Bi^{3+}, with its lone pair, evolves around the 000 position, inside the cube defined by O(1) oxygen atoms, with 4 Bi–O bonds shorter than 4 Bi–O long (mean 2.409 Å) involving a strong vibration ellipsoid for the O(1) atom.

TABLE 4
Anisotropic Displacement Parameters ($\times 10^4$) for $BiMn_6PO_{12}$

Atom	U_{11}	U_{22}	U_{33}	U_{12}	U_{13}	U_{23}
Bi	26(1)	$=U_{11}$	$=U_{11}$	0	0	0
Mn	30(2)	14(2)	$=U_{22}$	0	0	37(1)
P	8(2)	$=U_{11}$	$=U_{11}$	0	0	0
O(1)	49(4)	$=U_{11}$	$=U_{11}$	−15(4)	$=U_{12}$	$=U_{12}$
O(2)	13(5)	$=U_{11}$	$=U_{11}$	−5(5)	$=U_{12}$	$=U_{12}$

Note. The anisotropic temperature factor is defined by $\exp[-2\pi^2((U_{11}h^2a^{*2} + \cdots + 2U_{23}klb^*c^*)]$.

TABLE 5
Selected Distances (Å) and Angles (°) in $BiMn_6PO_{12}$

	Bi environment		
Bi–O(1)	2.409(6) (8×)		
	Mn environment		
		O(1)–Mn–O(1)	88.2(3)
Mn–O(1)	1.999(6) (4×)	O(1)–Mn–O(1)	91.8(3)
Mn–O(2)	2.331(7) (2×)	O(1)–Mn–O(2)	74.8(3)
		O(2)–Mn–O(2)	135.7(3)
	P environment		
P–O(2)	1.524(7) (4×)	O(2)–P–O(2)	109.5(5)
	Oxygen–oxygen distances		
O(1)–O(1)	2.782(12)	Mn–O(1)–Mn	116.7(2)
O(1)–O(1)	2.872(12)	Bi–O(1)–Mn	100.7(1)
O(1)–O(2)	2.643(9)		
O(2)–O(2)	2.488(13)		

The O(2) atoms of PO_4 tetrahedra complete the coordination of the Mn atom to form a distorted octahedron. The MnO_6 octahedron is elongated with the apical oxygen atoms O(2) at distances of 2.331 Å, longer than the four equatorial ones, 1.999 Å, leading to an averaged Mn–O distance of 2.11 Å, which matches very well with the weighted average $\frac{2}{3}(r\mathrm{Mn}^{3+} + r0^{2-}) + \frac{1}{3}(r\mathrm{Mn}^{2+} + r0^{2-}) = 2.09$ Å (26).

The distorted octahedral coordination of the Mn site is suitable to the Jahn–Teller nature of the Mn^{3+} ions; in contrast, for high-spin Mn^{2+}, the distortion cannot be ascribed to Jahn–Teller effects. However, some distorted environments around Mn^{2+} have already been observed, such as in $CeMn_2Ge_4O_{12}$ (27).

Bond valence sum calculations for Mn (Table 6), considering either Mn^{2+}–O^{2-} or Mn^{3+}–O^{2-} parameters from Brown and Altermatt (28), are consistent with the formal oxidation state of Mn at + 2.67.

Two kinds of MnO_6 distorted octahedra are obtained according to the orientation of PO_4 tetrahedra occupying the two $Mn_{12}O_{24}$ clusters connected by the considered MnO_4 square. If the two PO_4 are in the same orientation, the O(2)–Mn–O(2) angle is 135.7(3)°; in the opposite case, the O(2)–Mn–O(2) angle is 180° (Fig. 4).

The mean structure can be considered as built from distorted MnO_6 octahedra. One octahedron is edge-shared to eight other octahedra to form a three-dimensional infinite cluster creating tetrahedral and cubic holes occupied by P and Bi atoms, respectively. Interstitial atoms Bi and P form a rock salt type sublattice.

In fact, the mean structure of $BiMn_6PO_{12}$ results from a very compact association of perfect PO_4 tetrahedra, regular BiO_8 cubes, and distorted MnO_6 octahedra.

It is also of interest to describe the structure of $BiMn_6PO_{12}$ using the concept of close packing. Two kinds

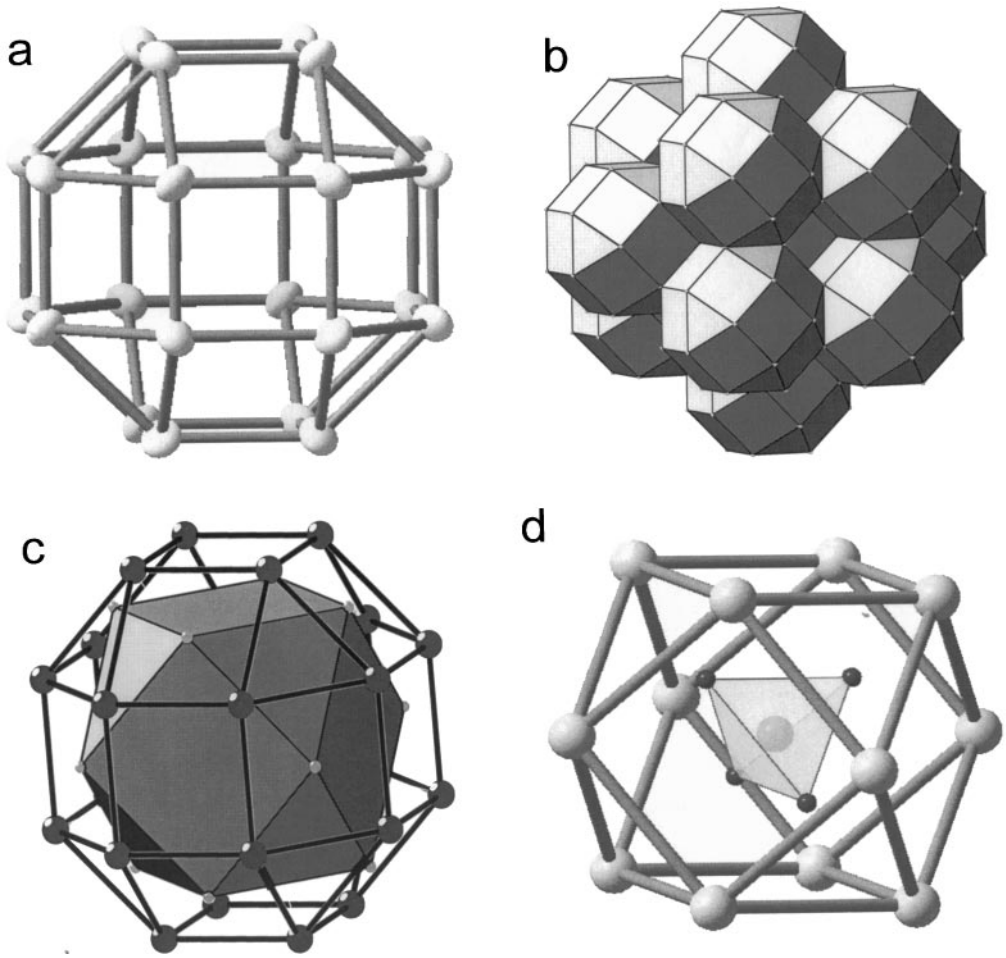

FIG. 2. The network in $BiMn_6PO_{12}$: (a) an outline of the rhombicuboctahedron formed from O(1) atoms. (b) A packing of the $O(1)_{24}$ rhombicuboctahedra. Each polyhedron is connected to 12 others by two-thirds of the square faces, those that share an edge with a triangular face. (c) These shared square faces are occupied by manganese atoms, forming a cuboctahedron. The manganese and O(1) oxygen atoms constitute a $Mn_{12}O_{24}$ entity. (d) The cuboctahedra are occupied by $PO(2)_4$ tetrahedra and the P–O(2) bonds are along the threefold axis of the polyhedra, so two equivalent orientations are possible for the PO_4 tetrahedra.

of layers are formed; layers **1** contain one P for three Mn atoms and layers **2** contain one Bi for three Mn atoms (Fig. 5). Layers **1** and **2** are stacked along the [111] direction of the cubic cell according to the cubic close packing (A**1**) (C**2**) (B**1**) (A**2**) (C**1**) (B**2**) sequence (Fig. 6). The oxygen atoms O(1) occupy two types of tetrahedral interstices created between the layers. The latter are formed by three Mn's of layer **2** and one Bi of layer **1**; the basal plane of the others is formed by two Mn's and one Bi of layer **1** and the apex is one Mn atom of layer **2**.

Thus, the O(1) atoms are coordinated by three manganese and one bismuth atoms, forming a tetrahedron. Eight $O(1)BiMn_3$ tetrahedra share the same bismuth atom. Each tetrahedron shares its Bi–Mn edges with three other tetrahedra to form a O_8BiMn_{12} entity; the 12 manganese atoms are at the vertices of a cuboctahedron.

TABLE 6
Bond Valence Sum Calculations for $BiMn_6PO_{12}$

	Mn^{2+}	Mn^{3+}
Mn–O(1)	0.572	0.527
Mn–O(2)	0.234	0.215
V_{Mn}	2.756	2.538

Electron Diffraction

The reconstitution of the reciprocal space confirms the lattice parameters ($a \approx 9.6$ Å) and the space group, but on some electron diffraction patterns, superimposed on the basic spots, weaker spots lead to multiply the cubic cell

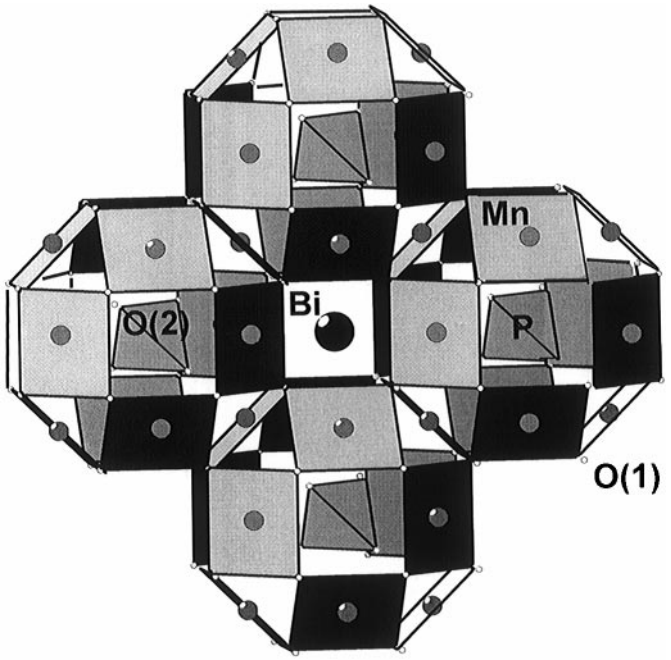

FIG. 3. Part of the framework of face-connected rhombicuboctahedra. The bismuth atoms lie at the centers of cubic holes resulting from the connection of six polyhedra.

parameter by two. The indexation of the electron diffraction patterns (EDPs) given for Figs. 7 and 8 are for the basic cubic unit cell. The [001] EDPs (Fig. 7a) do not show any weak spots responsible for the superstructure previously mentioned. But a rotation around the **a** direction exhibits planes where the weaker spots are easily visible. The arrows in the [031] (Fig. 7b) and [011] (Fig. 7c) EDP indicate these superstructure spots. The [110] EDPs (Fig. 8) of some crystals shows diffuse bands of intensity that have a periodic distribution (arrows). This feature indicates a short-range order. Nevertheless, a careful examination of the [011] EDPs of Fig. 7c reveals that the intensity of the weaker spots is different in the (111) direction and in the $(1\bar{1}\bar{1})$ direction, what would suppose twinning. A high-resolution electron microscopy study (actually in progress) is necessary, on one hand, to confirm this twinning and, on the other hand, to identify the structural origin of the superstructure phenomenon. So far, the latter is probably due to PO_4 and perhaps Bi ordering.

Magnetic Properties

Figure 9a shows the thermal evolution of the $BiMn_6PO_{12}$ magnetic susceptibility from room temperature down to 5 K. The material appears to be paramagnetic above 45 K, while a magnetically ordered state exists below. As observed in the Fig. 9a inset, the magnetic susceptibility gives evidence of several magnetic transitions between 2 and 50 K. The paramagnetic and ordered domains will be subsequently described as follows.

Paramagnetic state. The inverse of the molar magnetic susceptibility is shown in Fig. 9b. It obeys the Curie-Weiss law above 125 K, yielding $C_1 = 20.26$ emu K mol^{-1} and $\theta_{C1} = -51.3$ K. The calculated effective moment $p_{eff} = 12.73\ \mu_B$ f u^{-1} is in good agreement with the predicted value 12.88, assuming a spin-only J value for two high-spin Mn^{2+} and four high-spin Mn^{3+}, likely for both cations. Antiferromagnetic Mn–Mn interactions are then expected to predominate, hence the negative Weiss temperature. The gradual increasing of the $\chi \cdot T$ product versus T confirms the AF couplings. An anomaly in χ^{-1} versus T is evidenced around 125 K where the slope progressively increases to reach a second linear regime between 110 and 30 K. In that region the Curie–Weiss law yields $C_2 = 11.77$ emu K mol^{-1} and $\theta_{C2} = 23.6$ K, leading to $p_{eff} = 9.70\ \mu_B$ f u^{-1}. This phenomenon is associated with an abrupt change in the $\chi \cdot T$ product. Several electronic configurations were supposed to explain such a value; among them only a two high-spin Mn^{2+} ($t_{2g}^3 e_g^2$, $S = 5/2$)/four low-spin Mn^{3+} ($t_{2g}^4 e_g^0$, $S = 1$) main configuration was retained involving the theoretical 10.09 μ_B f u^{-1} in a spin-only approximation. Among the several cases of high-spin states for both Mn^{2+} and Mn^{3+} (i.e., see Refs. (29–31)), we did not find in the literature any example of high-spin → low-spin transition for the latter in oxides that one should consider only as an hypothetical suggestion. Therefore, one should notice that an octahedral Mn^{3+} spin crossover was observed in manganese tris[1-(2-azolyl)-2-azabuten-4-yl]

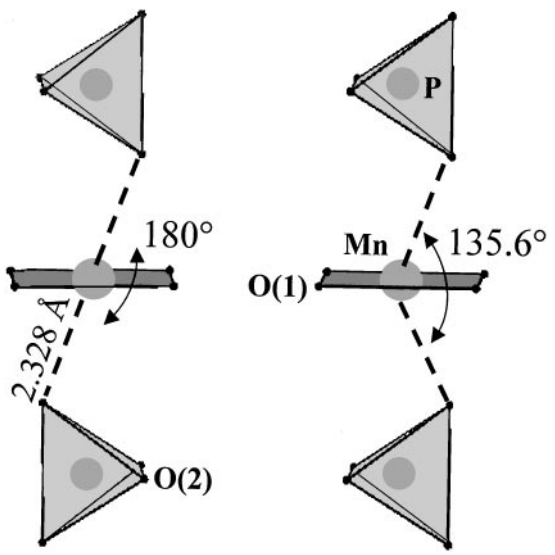

FIG. 4. The two kinds of distorted MnO_6 octahedra according to the occupation of two square face-shared rhombicuboctahedra by two PO_4 tetrahedra in the same orientation (left) or in two different orientations related by an inversion center (right).

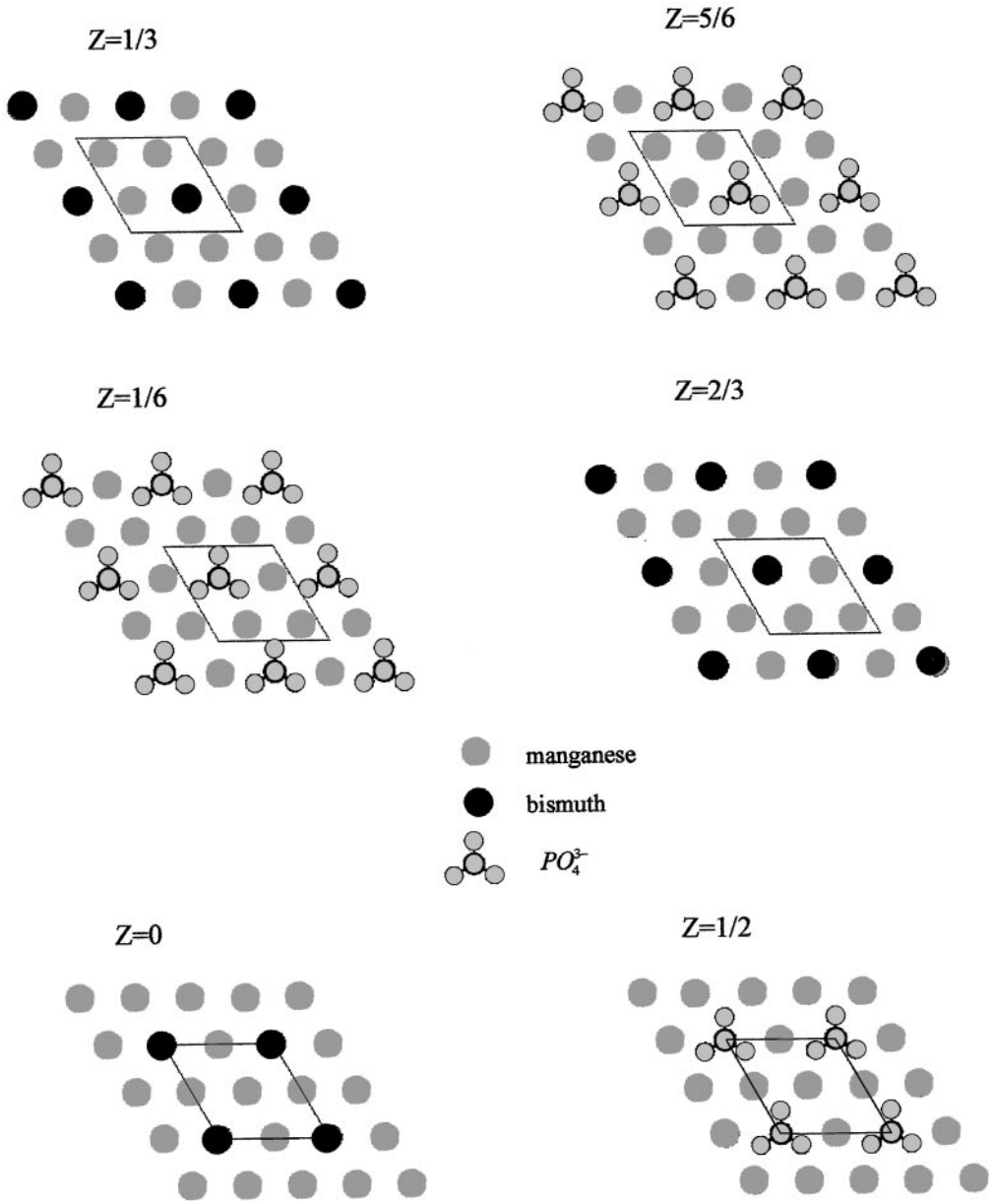

FIG. 5. The $Mn_3(PO_4)$ (**1**) and Mn_3Bi (**2**) close-packed layers in the $BiMn_6PO_{12}$ structure described in the hexagonal unit cell deduced from the cubic one by the relation

$$\begin{pmatrix} a_{\text{hex}} \\ b_{\text{hex}} \\ c_{\text{hex}} \end{pmatrix} = \begin{pmatrix} -\frac{1}{2} & \frac{1}{2} & 0 \\ 0 & -\frac{1}{2} & \frac{1}{2} \\ 1 & 1 & 1 \end{pmatrix} \begin{pmatrix} a_{\text{c}} \\ b_{\text{c}} \\ c_{\text{c}} \end{pmatrix}.$$

The z values are for the hexagonal axis.

amine in which the ligand field is much higher than that in oxides (32). As seen in the structural section, at room temperature, both Mn^{2+} and Mn^{3+} occupy the same independent 24*d* crystallographic position while a low-temperature electronic configuration segregation between both species strongly suggest a crystallographic distinction between both, possibly arising from a structural distortion and/or a charge ordering.

Ordered state. The Neel temperature is evidenced by a sharp peak at 20 K surrounded by two extra magnetic transitions. A first phenomenon is observed at 42 K during

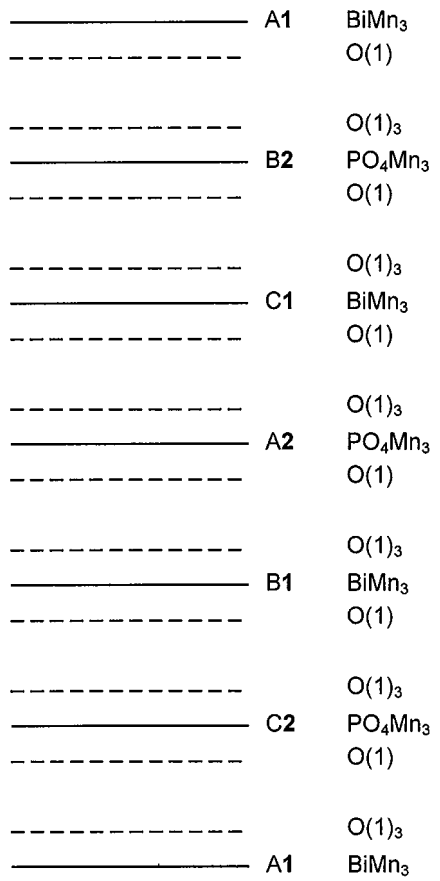

FIG. 6. The layer stacking sequence along the [111] direction of the cubic unit cell of $BiMn_6PO_{12}$.

the increasing of the susceptibility upon cooling. Several measurements performed on different samples confirm the reproducibility of the slight χ deviation not assigned so far. Below T_N, the susceptibility is decreasing down to 6 K to a constant value of 1.15 emu mol^{-1} and then rapidly collapses at lower temperatures. A magnetic transition is then expected at 16 K. Magnetization versus the applied field was measured at 40, 20, and 2 K, respectively to distinguish between the subsequent thermal regions. Results are presented in the Figs. 10a–10c. At 40 and 20 K the magnetization plots are characteristic of the setting of an antiferromagnetic ordering before and below T_N. No hysteresis loops are observed and the plot changes from almost linear at 20 K to a concave upward shape at 40 K. Considering the $BiMn_6PO_{12}$ crystal structure, it seems difficult to predict the exchange interactions according to Kanomori–Goodenough semi-empirical rules (33). Considering the Mn–Mn distances of 3.39 Å, direct exchanges are excluded and the main antiferromagnetic should arise from the competition of the Mn^{2+}–O–Mn^{3+}, Mn^{2+}–O–Mn^{2+}, and Mn^{3+}–O–Mn^{3+} superexchanges, in a localized electrons consideration. Because of the mixed Mn^{2+}/Mn^{3+} valence, double exchange cannot be totally excluded but since they are ferromagnetic we will not consider them in the following discussion. The O(2) atom is strongly involved in a P–O(2) bond, 1.524(7) Å, and form a weak Mn–O(2) bond, 2.331(7) Å, as compared to Mn–O(1), 1.999(6) Å. Thus, the latter should strongly intervene in the magnetic path. O(1) is at the center of a distorted $O(1)BiMn_3$ tetrahedron with a Mn–O–Mn angle of 116.7° and can be regarded as being in an intermediate state between sp^2 and a sp^3 hybridization because of the flat $O(3)Mn_3$ trigonal pyramid with either

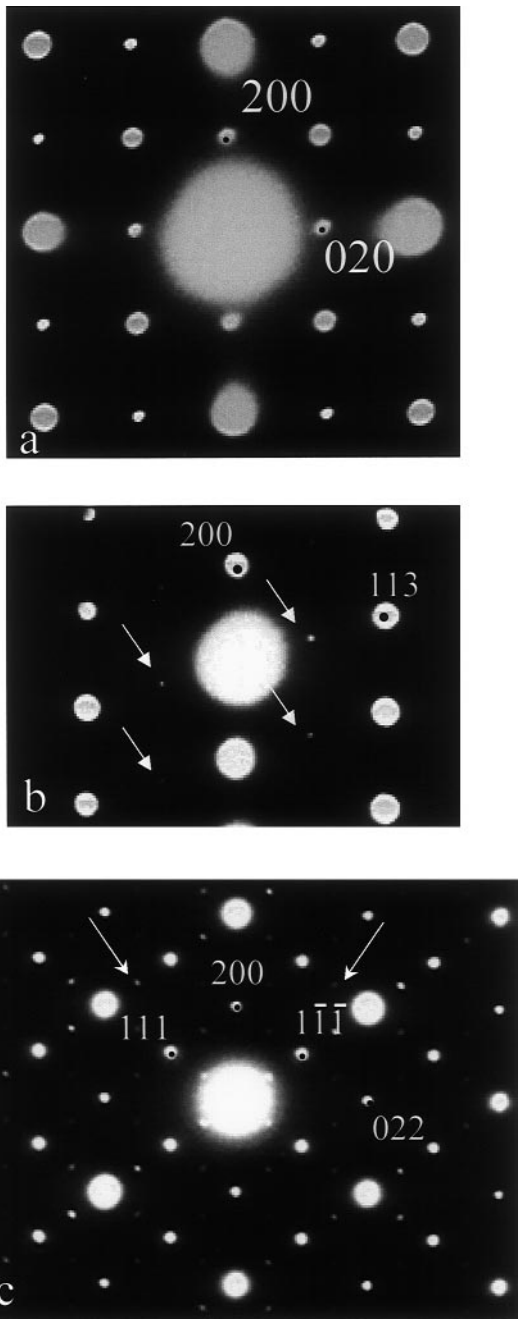

FIG. 7. (a) [001] EDP pattern, the superstructure is not visible. (b) [031] and (c) [011] EDP; arrows indicate superstructure spots.

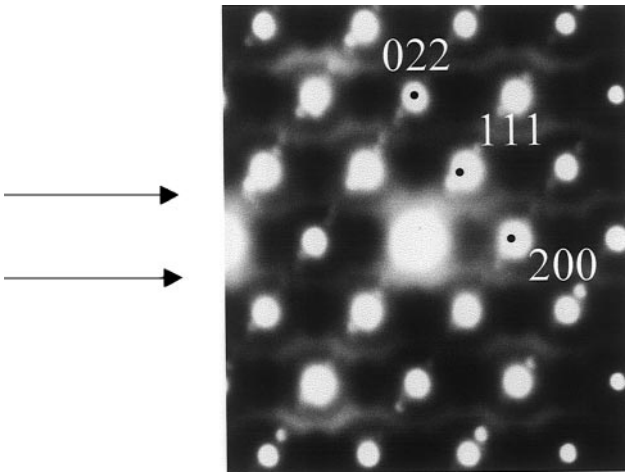

FIG. 8. [110] EDP of some crystals of $BiMn_6PO_{12}$; diffuse bands of intensity are observed (arrows).

three sp^2_σ overlapping the Mn e_g orbitals and $p_z\sigma$ pointing toward Bi (theoretical Mn–O–Mn of 120°), Fig. 11, or four $sp^3\sigma$ orbitals pointing toward the four ligands (theoretical Mn–O–Mn of 109°). In any case, the Mn–Mn magnetic exchanges are likely effective via e_g-sp^2_σ–sp^2_σ-e_g double-correlation superexchanges. Exchange integrals signs are predicted positive for d^4–d^4 and d^5–d^5 interactions and negative for d^4–d^5 interactions in a 90° M–O–M configuration. Each Mn site is surrounded by eight Mn at 3.39 Å. Thus, a competition between positive and negative exchanges should occur in a 1/1 ratio considering two-thirds of the cases consisting of one central Mn^{3+} surrounded by five Mn^{3+} and three Mn^{2+} and one-third of the cases consisting of one central Mn^{2+} surrounded by six Mn^{3+} and one Mn^{3+}. Such competition is hardly to be seen on the rhombicuboctahedron without involving strong frustration, hence the magnetic structure.

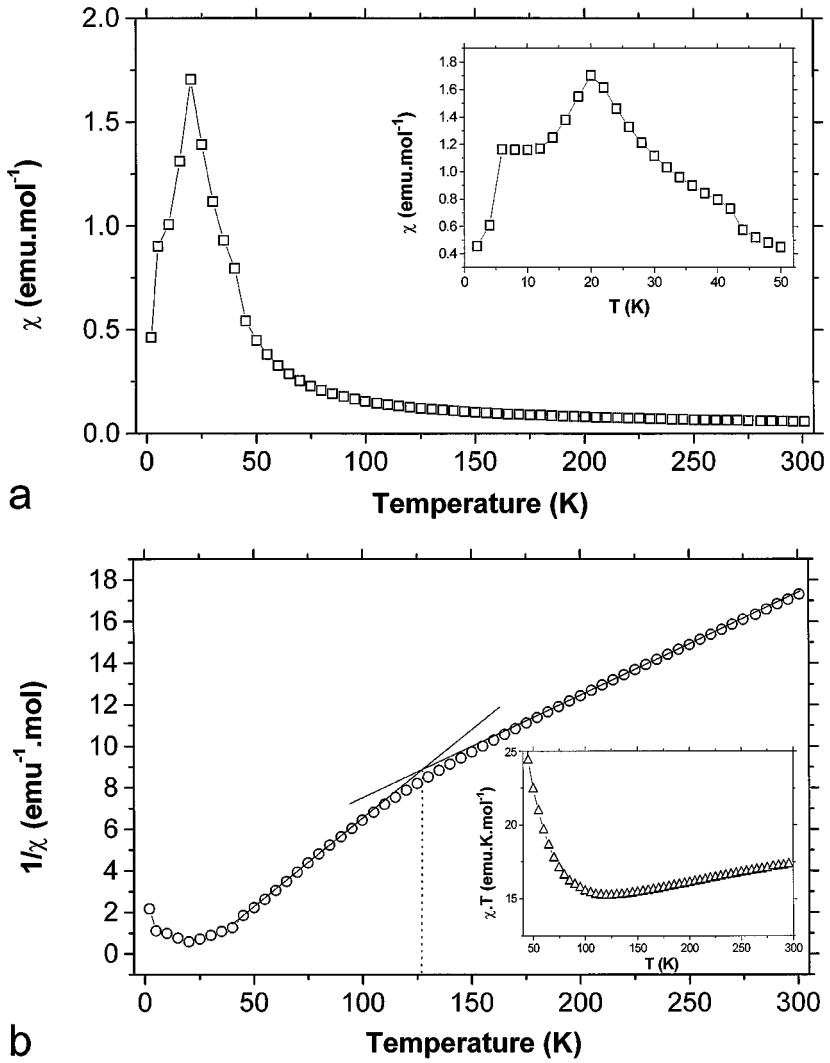

FIG. 9. The thermal evolution of the magnetic susceptibility for $BiMn_6PO_{12}$. (a) Variation of χ versus T. The inset highlights three anomalies in the low-temperature domain. (b) The χ inverse versus temperature. The straight lines evidence the slope change occurring around 125 K. This phenomenon is assorted with a drastic change of the $\chi \cdot T$ product shown in the inset.

Below 6 K a magnetic transition is observed. The magnetization plot measured at 2 K is drastically different from that of a pure antiferromagnet. It shows a remanent magnetization of 0.75 μ_B f u^{-1}. The discrepancy observed at the zero field is probably due to rotation of the grains within the sample. The spontaneous moment may be caused by the setting of a ferrimagnetic ordering below 6 K. A canted structure may also appear at low temperature.

CONCLUSION

A new oxyphosphate of bismuth and manganese has been synthesized. Its original structure is highly symmetric and can be described from a cubic three-dimensional network of manganese and oxygen atoms, creating two kinds of cavities occupied by PO_4 tetrahedra and Bi atoms, respectively. The mean oxidation state of manganese atoms, which are crystallographically equivalent, is + 2.67. Magnetic measurements revealed transitions both in the paramagnetic and in the ordered states. Further studies are planned to complete the reported structural approach, in particular, low- and high-temperature X-ray/neutron diffraction as well as EPR experiments to explain both the superstructure observed by electronic diffraction and the different magnetic structures of this fascinating new material. Substitutions for Bi by isovalent (Ln^{3+}) or aliovalent ions such as Pb^{2+} or Na^{+} whose radii are compatible with the size of the cube formed by the O(1) atoms are also to be considered. The latter substitutions should modify the mean oxidation state of manganese and as a consequence the magnetic behavior of the prepared compounds.

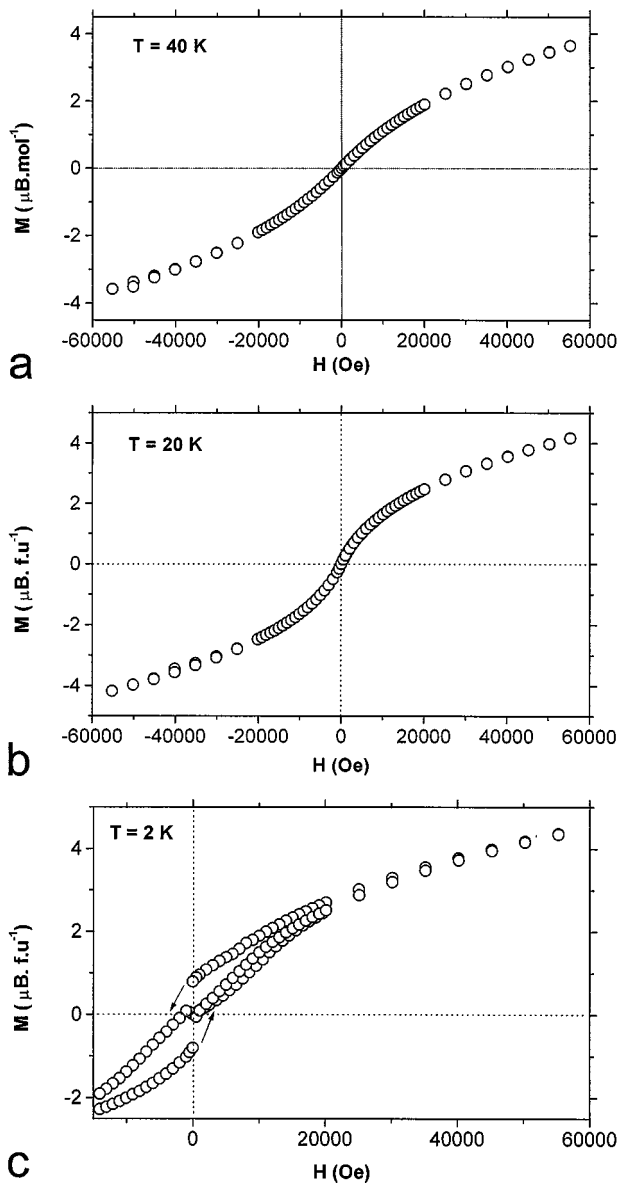

FIG. 10. Magnetization versus applied field at (a) 40 K (b) 20 K and (c) 2 K.

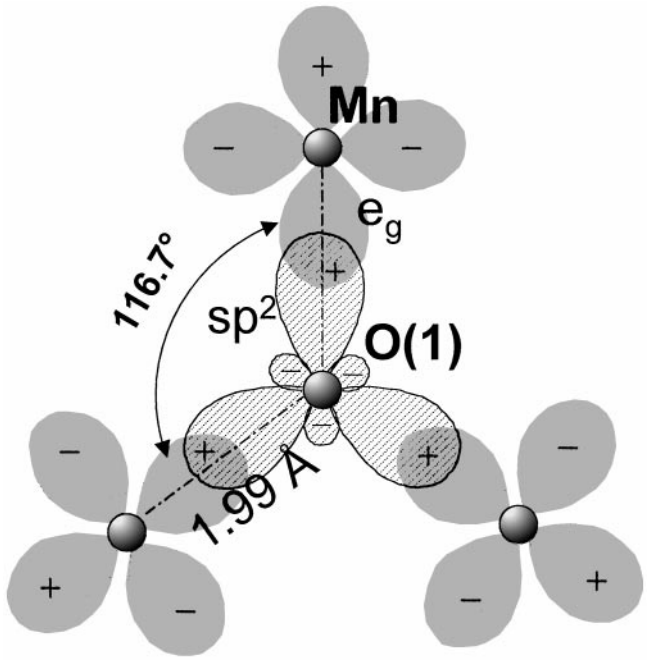

FIG. 11. Schematic hybridized orbitals model of a Mn–O–Mn double-correlation superexchange path.

REFERENCES

1. J. C. Boivin, J. Trehoux, and D. Thomas, *Bull. Soc. Fr. Minéral. Cristallogr.* **99,** 193 (1976).
2. F. Abraham, M. F. Debreuille-Gresse, G. Mairesse, and G. Nowogrocki, *Solid State Ionics* **28–30,** 529 (1988).
3. F. Abraham, J. C. Boivin, G. Mairesse, and G. Nowogrocki, *Solid State Ionics* **40/41,** 934 (1990).
4. M. Ketatni, Ph.D. dissertation, Université des Sciences et Technologies de Lille, April 1995.

5. F. Abraham, M. Ketatni, and B. Mernari, *Adv. Mater. Res.* **1–2,** 223 (1994).
6. F. Abraham, M. Ketatni, G. Mairesse, and B. Mernari, *Eur. J. Solid State Inorg. Chem.* **31,** 313 (1994).
7. J. Huang and A. W. Sleight, *J. Solid State Chem.* **100,** 170 (1992).
8. J. Huang, Q. Gu, and A. W. Sleight, *J. Solid State Chem.* **105,** 599 (1993).
9. I. Radosavljevic, J. S. O. Evans, and A. W. Sleight, *J. Solid State Chem.* **141,** 149 (1998).
10. M. Ketatni, B. Mernari, F. Abraham, and O. Mentre, *J. Solid State Chem.* **153,** 48 (2000).
11. I. Radosavljevic, J. S. O. Evans, and A. W. Sleight, *J. Solid State Chem.* **137,** 143 (1998).
12. N. Tancret, Ph.D. dissertation, Université des Sciences et Technologies de Lille, September 1995.
13. A. Mizrahi, J. P. Wignacourt, and H. Steinfink, *J. Solid State Chem.* **133,** 516 (1997).
14. I. Radosavljevic, J. S. O. Evans, and A. W. Sleight, *J. Alloys Compd.* **284,** 99 (1999).
15. B. Serien-Verdonck, Ph.D. dissertation, Université des Sciences et Technologies de Lille, September 1991.
16. G. B. Deacon, B. M. Gatehouse, and G. N. Ward, *Acta Crystallogr. C* **50,** 1178 (1994).
17. F. Abraham and M. Ketatni, *Eur. J. Solid State Inorg. Chem.* **32,** 429 (1995).
18. M. Ketatni, F. Abraham, and O. Mentre, *Solid State Sci.* **1**(6), 449 (1999).
19. S. Nadir, J. S. Swinnea, and H. Steinfink, *J. Solid State Chem.* **148,** 295 (1999).
20. "Colossal Magnetoresistance, Charge Ordering and Related Properties of Manganese Oxides." (C. N. R. Rao and B. Raveau, Eds.). World Scientific, Singapore, 1998.
21. G. Smith and R. J. Snyder, *J. Appl. Crystallogr.* **12,** 60 (1979).
22. G. M. Sheldrick, "SHELXS-86, Program for Crystal Structure Determination." University of Göttingen, Germany, 1986.
23. C. T. Prewitt, SFLS-5, Report ORNL-TM 305, Oak Ridge National Laboratory, Oak Ridge, TN, 1966.
24. "International Tables for X-Ray Crystallography," Vol. IV. Kynoch Press, Birmingham, UK, 1974.
25. D. T. Cromer and D. Liberman, *J. Chem. Phys.* **53,** 1891 (1970).
26. R. D. Shannon, *Acta Crystallogr Sect. A* **32,** 751 (1976).
27. C. Travio-Guého, P. Léone, P. Palvadeau, and J. Rouxel, *J. Solid State Chem.* **143,** 145 (1999).
28. I. D. Brown and D. Altermatt, *Acta Crystallogr. Sect. B* **41,** 244 (1985).
29. J. H. Liao, F. Leroux, C. Payen, D. Guyomard, and Y. Piffard, *J. Solid State Chem.* **121,** 214 (1996).
30. A. K. Pahdi, W. B. Archibald, K. S. Nanjundaswamy, and J. B. Goodenough, *J. Solid State Chem.* **128,** 267 (1997).
31. D. Pelloquin, C. Michel, A. Maignan, M. Hervieu, and B. Raveau, *J. Solid State Chem.* **138,** 278 (1998).
32. P. G. Sim and E. Sinn, *J. Am. Chem. Soc.* **103,** 243 (1981).
33. J. B. Goodenough, *in* "Magnetism and the Chemical Bond." p. 165, Interscience, New York, 1963.